Monthly Notices
of the
ROYAL ASTRONOMICAL SOCIETY

MNRAS **485,** 2054–2070 (2019)
Advance Access publication 2019 February 22

doi:10.1093/mnras/stz523

Gemini NIFS survey of feeding and feedback in nearby active galaxies – III. Ionized versus warm molecular gas masses and distributions

Astor J. Schönell, Jr.,[1,2★] Thaisa Storchi-Bergmann,[1★] Rogemar A. Riffel,[3★] Rogério Riffel,[1] Marina Bianchin,[3] Luis G. Dahmer-Hahn,[1] Marlon R. Diniz[3] and Natacha Z. Dametto[1]

[1]*Instituto de Física, Universidade Federal do Rio Grande do Sul, Av. Bento Gonçalves 9500, 91501-970 Porto Alegre, RS, Brazil*
[2]*Instituto Federal de Educação, Ciência e Tecnologia Farroupilha, BR287, km 360, Estrada do Chapadão, 97760-000 Jaguari, RS, Brazil*
[3]*Departamento de Física, Universidade Federal de Santa Maria, Centro de Ciências Naturais e Exatas, 97105-900 Santa Maria, RS, Brazil*

Accepted 2019 February 16. Received 2019 February 15; in original form 2017 August 15

ABSTRACT

We have used the Gemini Near-Infrared Integral Field Spectrograph in the *J* and *K* bands to map the distribution, excitation, and kinematics of the ionized H II and warm molecular gas H_2, in the inner few 100 pc of six nearby active galaxies: NGC 788, Mrk 607, NGC 3227, NGC 3516, NGC 5506, NGC 5899. For most galaxies, this is the first time that such maps have been obtained. The ionized and H_2 gas show distinct kinematics: while the H_2 gas is mostly rotating in the galaxy plane with low velocity dispersion (σ), the ionized gas usually shows signatures of outflows associated with higher σ values, most clearly seen in the [Fe II] emission line. These two gas species also present distinct flux distributions: the H_2 is more uniformly spread over the whole galaxy plane, while the ionized gas is more concentrated around the nucleus and/or collimated along the ionization axis of its active galactic nucleus (AGN), presenting a steeper gradient in the average surface mass density profile than the H_2 gas. The total H II masses cover the range 2×10^5–2×10^7 $M_\odot$, with surface mass densities in the range 3–150 $M_\odot$ pc^{-2}, while for the warm H_2 the values are 10^{3-4} times lower. We estimate that the available gas reservoir is at least $\approx$100 times more massive than needed to power the AGN. If this gas forms new stars the star formation rates, obtained from the Kennicutt–Schmidt scaling relation, are in the range 1–260 $\times 10^{-3}$ $M_\odot$ yr^{-1}. But the gas will also – at least in part – be ejected as the observed outflows.

Key words: galaxies: active – galaxies: evolution – galaxies: kinematics and dynamics – galaxies: nuclei – galaxies: Seyfert – galaxies: star formation.

1 INTRODUCTION

The growth of supermassive black holes (SMBH) and their host galaxies are connected by the active galactic nucleus (AGN) feeding and feedback processes that can presumably explain the correlation between the mass of the SMBH and the mass of the galaxy bulge (Ferrarese & Ford 2005; Somerville et al. 2008; Kormendy & Ho 2013). The feeding via gas accretion is required to trigger the nuclear activity, while the feedback provided by the AGN radiation and outflows is fundamental to constrain galaxy evolution models, since without the AGN feedback the models predict that the most massive galaxies form too many stars and grow more than observed (Springel, Di Matteo & Hernquist 2005; Fabian 2012; Terrazas et al. 2016).

Gas distribution, excitation, and kinematics in the vicinity of AGNs ($\approx$100 pc scales) provide important constraints on the physics of the AGN feeding and feedback processes. The near-infrared (hereafter, near-IR) integral field spectroscopy (IFS) of nearby galaxies is an effective method to quantify these processes. 8–10 metre telescopes IFS with adaptive optics (AO) can provide two-dimensional coverage with spatial resolution of a few to tens of parsecs in nearby galaxies at spectral resolutions that allow to resolve gas inflows and outflows at such scales (Müller Sánchez et al. 2009; Davies et al. 2009, 2014). AO systems are available mainly in the near-IR, a spectral region that also has the advantage of being

★ E-mail: juniorfisicoo@gmail.com (AJSJr); thaisa@ufrgs.br (TS-B); rogemar@ufsm.br (RAF)

less affected by dust extinction (usually high in the central region of galaxies) than optical observations. The use of AO assisted IFS of nearby galaxies in the near-IR thus allows to resolve the central regions down to a few parsecs, and also simultaneously map two distinct gas phases: the ionized and molecular (H_2) gas emission. The latter is not available in the optical but can be observed in the near-IR *K* band.

The near-IR line emission at ≈100 pc scales in AGN hosts is originated by the heating and ionization of ambient gas by the AGN radiation and by shocks produced by radio jets (Riffel et al. 2006; Riffel, Storchi-Bergmann & Nagar 2010a). Recent observations by our group AGNIFS – AGN Integral Field Spectroscopy (e.g. Riffel et al. 2018) and others show that the molecular and ionized gas have distinct spatial distributions and kinematics at these scales: the former is usually more restricted to the plane of galaxies, with the kinematics being dominated by rotation in the disc in most cases, and presenting also signatures of inflows in some cases; the latter traces a more disturbed medium, usually associated with outflows from the AGN, but frequently showing also a disc rotation component (e.g. Riffel et al. 2010a; Riffel, Storchi-Bergmann & Winge 2013; Barbosa et al. 2014; Mazzalay et al. 2014; Diniz et al. 2015). Our previous studies led to the conclusion that, while the ionized gas emission can be considered a tracer of the AGN feedback, the molecular gas emission is usually a tracer of its feeding.

In this paper we present maps of the ionized and molecular gas distribution, excitation, and kinematics of the inner 3 × 3 arcsec^2 of a sample of six nearby Seyfert galaxies. The discussion is restricted to the gas mass distributions and total ionized and molecular gas masses as well as to the presentation of the global gas kinematics, pointing out signatures of rotation and outflows. The analysis and discussion of the gas excitation as well as the modelling of the gas kinematics and quantification of outflows will be deferred to a forthcoming paper (hereafter identified as Paper B). This work is the third paper with the results of a large Gemini proposal (P.I. Storchi-Bergmann) in which our group AGNIFS aims to map and quantify the feeding and feedback processes of a sample of 29 nearby Seyfert galaxies (Riffel et al. 2018), selected for their proximity and X-ray luminosity, as described in Section 2. Our ultimate goal is to investigate possible correlations between measured properties (as gas masses and densities, mass inflow and outflow rates, and kinetic power of the outflows) and the AGN luminosity. Results for individual galaxies of the sample have been already presented in previous papers by our group: NGC 4051 (Riffel et al. 2008a, 2017), NGC 4151 (Riffel et al. 2009a; Storchi-Bergmann et al. 2009, 2010), Mrk 1066 (Ramos Almeida et al. 2009; Riffel et al. 2010b; Riffel & Storchi-Bergmann 2011a; Riffel et al. 2017), Mrk 1157 (Riffel & Storchi-Bergmann 2011a; Riffel et al. 2011b, 2017), NGC 1068 (Barbosa et al. 2014; Riffel et al. 2014a; Storchi-Bergmann et al. 2012), Mrk 79 (Riffel et al. 2013), Mrk 766 (Schönell et al. 2014; Riffel et al. 2017), NGC 5929 (Riffel, Storchi-Bergmann & Riffel 2014b, 2015; Riffel et al. 2017), NGC 2110 (Diniz et al. 2015), NGC 5548 (Riffel et al. 2017; Schönell et al. 2017), NGC 788, NGC 3227, NGC 3516, NGC 4235, NGC 4388, NGC 5506, NGC 1052, NGC 5899, and Mrk 607 (Riffel et al. 2017).

This paper is organized as follows. In Section 2 we present the sample and in Section 3 the description of the observations and data reduction procedures, while the fitting procedure of the emission lines is discussed in Section 4. The results are shown in Section 5, we discuss them in Section 6, and in Section 7 we present our conclusions.

2 SAMPLE

Our AGN sample was selected from the *Swift*-BAT 60-month catalogue adopting three criteria: (i) 14–195 keV luminosities $L_X \geq 10^{41.5}$ erg s^{-1}, (ii) redshift $z \leq 0.015$, and (iii) being accessible for Near-Infrared Integral-Field Spectrograph (NIFS) ($-30^\circ < \delta < 73^\circ$). The selection according to the hard (14–195 keV) band emission of the *Swift*-BAT survey is justified by the fact that it measures direct emission from the AGN rather than scattered or reprocessed emission, and is much less sensitive to obscuration in the line of sight than soft X-rays or optical observations, allowing a selection based only on the AGN properties. In order to assure that we will be able to probe the feeding and feedback processes we further selected the galaxies for having previously observed extended [O III] λ5007 emission (Schmitt & Kinney 2000), which enhances the probability of them presenting extended near-IR line emission, needed to map the gas excitation and kinematics. We have excluded a few galaxies that had guiding problems in the observations and included additional targets from our previous NIFS observations to complement the sample, leading to a total sample of 29 active galaxies. A complete characterization of the sample has been presented in Riffel et al. (2018). The observations are still in progress and will probably be concluded in 2019. So far, 20 galaxies have been observed and here we show the gas distribution and excitation for six of them. These six galaxies are listed in Table 1, which presents also their nuclear activity type, morphological classification, and information about the observations.

3 OBSERVATIONS AND DATA REDUCTION

We used *J*- and *K*-band data obtained with the Gemini NIFS (McGregor et al. 2003) with the AO system ALTAIR between 2008 and 2016. NIFS has a square field of view (FOV) of 3 × 3 arcsec^2, divided into 29 slitlets 0.″103 wide with a spatial sampling of 0.″042 along them. We used the standard Sky–Object–Object–Sky dither sequence in the observations, with off-source sky positions since all targets are extended. The individual exposure times varied according to the target and are listed, together with further information on the observations in Table 1. The filter ZJ_G0601 was used with the *J*-band observations, while the *K*-band observations were performed using the HK_G0603 filter, as shown in Table 2 together with further details of the instrument configuration.

Data reduction followed standard procedures and was accomplished using tasks specifically developed for NIFS data reduction, as part of GEMINI IRAF package, as well as generic IRAF tasks and IDL scripts. The procedures included trimming of the images, flat-fielding, sky subtraction, wavelength, and s-distortion calibrations. The telluric absorptions have been removed using A-type standard stars observations. These stars were also used to flux calibrate the spectra of the galaxies by interpolating a blackbody function to the spectrum of each star in order to generate the sensitivity function. Finally, calibrated data cubes were created for each individual exposure at an angular sampling of 0.″05 × 0.″05 and combined in a final data cube for each galaxy. All data cubes cover the inner ≈3.″0 × 3.″0 and have typical spectra as shown in Fig. 1. As shown in Riffel et al. (2018), the spectral resolutions for both bands correspond to velocities of about 40 km s^{-1} and the angular resolution ranges from 0.″12 to 0.″18, corresponding to a few tens of parsecs at the galaxies.

Table 1. Log of the observations together with basic information on the sample galaxies. (1) Galaxy name; (2) Project ID; (3) *J*- and (4) *K*-band exposure times (s); (5) Distance (Mpc); (6) Nuclear Activity; (7) Hubble type from NED; (8) Scale; (9) AGN bolometric luminosity.

1 Galaxy	2 Project ID	3 J Exp-time (sec)	4 K Exp-time (sec)	5 D (Mpc)	6 Act.	7 Hub. type	8 Scale (pc arcsec^{-1})	9 logL_{AGN} (erg s^{-1})
NGC 788	GN-2015B-Q-29	7 × 400	11 × 400	56.1	Sy2	SA0/a(s)	272	44.4
Mrk607	GN-2012B-Q-45	10 × 500	12 × 500	36.1	Sy2	Sa edge-on	175	–
NGC 3227	GN-2016A-Q-6	6 × 400	6 × 400	14.8	Sy1.5	SAB(s)a pec	72	43.4
NGC 3516	GN-2015A-Q-3	10 × 450	10 × 450	38.0	Sy1.5	(R)SB0^0(s)	184	44.2
NGC 5506	GN-2015A-Q-3	10 × 400	10 × 400	24.9	Sy1.9	Sa pec edge-on	121	44.3
NGC 5899	GN-2013A-Q-48	10 × 460	10 × 460	36.8	Sy2	SAB(rs)c	178	43.1

Table 2. Configuration of the observations: (1) spectral band, (2) grating, (3) filter, (4) filter central wavelength, (5) filter spectral range, (6) galaxies observed in each configuration.

Band	Grating	Filter	Central Wav. (μm)	Spec. Range (μm)	Galaxies observed
J	J_G5603	ZJ_G0601	1.25	1.14–1.36	All
K	K_G5605	HK_G0603	2.20	1.98–2.40	NGC 788, NGC 3516, and NGC 5506
K_l	Kl_G5607	HK_G0603	2.30	2.08–2.50	Mrk 607, NGC 3227, and NGC 5899

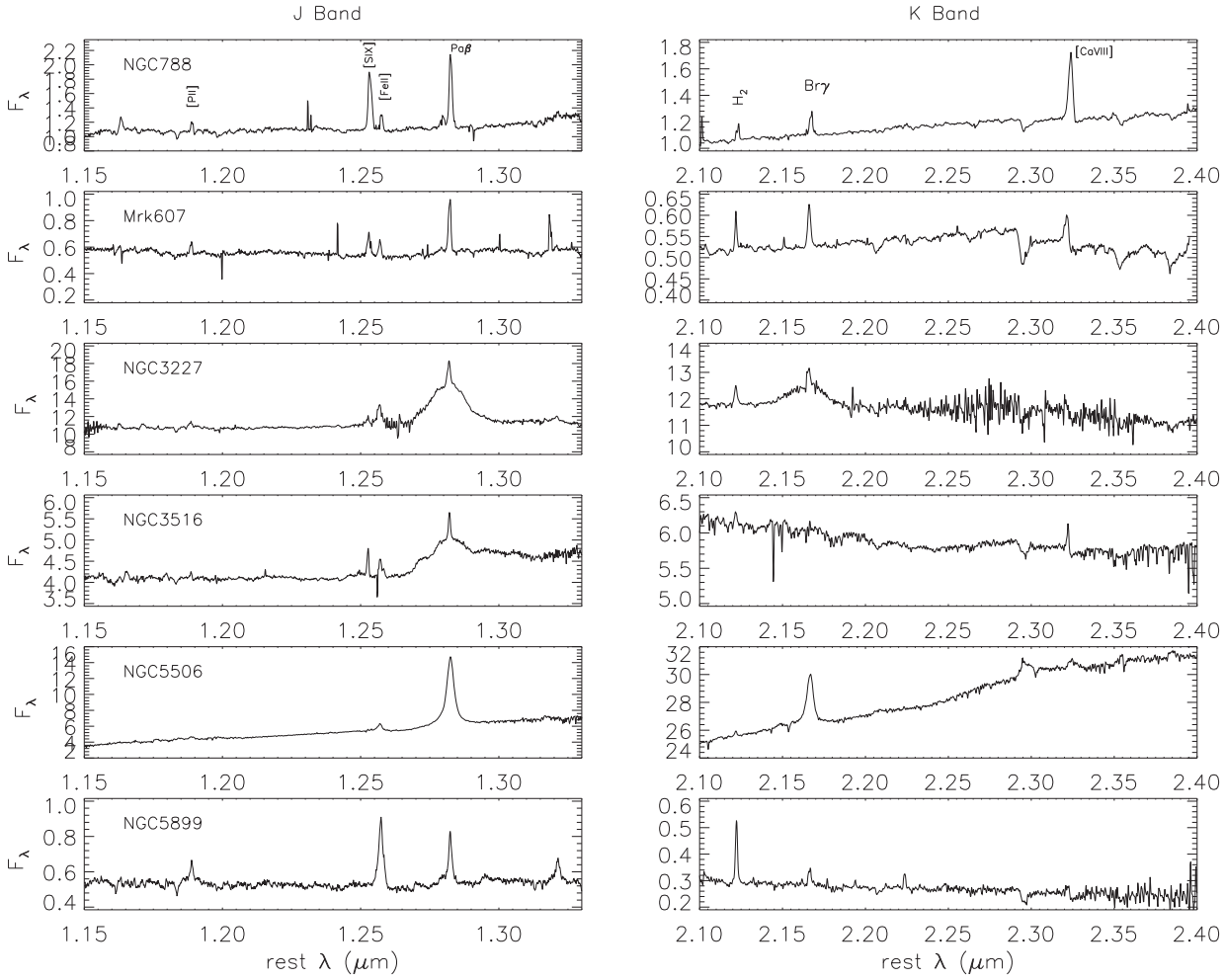

Figure 1. *J*-band (left) and *K*-band (right) spectra obtained within a 0.″25 × 0.″25 aperture centred at the nucleus of the galaxy indicated in the top left corner of the left-hand panels. Flux units are 10^{-16} erg s^{-1} cm^{-2} Å^{-1}.

4 MEASUREMENTS

We have used the PROFIT routine (Riffel 2010) to fit the profiles of the following emission lines at each pixel over the whole FOV: [P II] λ1.1886 μm, [Fe II] λ1.2570 μm, Pa βλ1.2822 μm, H_2λ2.1218 μm, and Br γλ2.1661 μm. This was done using Gauss–Hermite series, which were chosen to preserve most of the gas velocity information by fitting also the emission line wings via the moments h_3 and h_4, besides returning the line-of-sight velocity (V_{LOS}) and velocity dispersion (σ).

The h_3 Gauss–Hermite moment measures asymmetric deviations from a Gaussian profile, such as blue (negative values) or red (positive values) wings, while the h_4 moment quantifies the peakness of the profile, with positive values for a more peaked profile and more extended wings than a Gaussian and negative values for a broader profile (more flat topped) and with less extended wings than that of a Gaussian curve.

The underlying continuum was fitted using a first degree function, since the spectral range used in the fit of each emission line was small. The routine uses the MPFITFUN routine (Markwardt 2009) to perform a non-linear χ^2 minimization. The fit of the line plus continuum involves seven free parameters – line amplitude, central wavelength, σ, h_3, h_4 plus another two from the first degree function used to fit the continuum. The only restrictions placed are that $|h_3|$ and $|h_4|$ are <0.5, but most returned values are smaller than these. Actually, this restriction was hardly used, as values 0.5 or higher indicate profiles that are very distinct from Gaussian curves, which are not observed in the galaxies' spectra. The PROFIT routine also outputs 1σ errors for each of the parameters, computed from the covariance matrix.

In the case of NGC 3227, NGC 3516, and NGC 5506 we also fitted a broad component to the Pa β and Br γ emission line profiles in the central region, as these galaxies host type 1 AGN. This was done through a modification of the PROFIT routine to fit the broad component and subtract its contribution from the profiles in order to generate a data cube only with the narrow components. The steps for such task were: (i) fit of only one Gaussian to the broad component, by masking strong narrow emission lines; (ii) its subtraction from the spectra in which it is present, and (iii) fit of the narrow components. We achieved very satisfactory fits in all cases, with no constraints placed for the fit. The spatial region within which the fit of a broad component was necessary is shown by a cyan square in the third panel of the first row in Figs 4, 5, and 6, respectively, for NGC 3227, NGC 3516, and NGC 5506. As the broad components are from the unresolved broad-line region (BLR), during the fit we kept fixed the central wavelength and width of the broad components to the value measured from the integrated spectrum within the square mentioned above and allowed only the variation of its amplitude. From the measurements presented in Figs 4, 5, and 6, we conclude that the subtraction of the broad components was satisfactory, as we found no traces of them in the subtracted data cube.

5 RESULTS

From the fits of the line profiles and resulting parameters we have constructed maps of: flux distributions, V_{LOS}, velocity dispersions, h_3 and h_4 moments as well as of the reddening $E(B-V)$ and emission line ratio maps, presented in Fig. 2 for NGC 788, Fig. 3 for Mrk 607, Fig. 4 for NGC 3227, Fig. 5 for NGC 3516, Fig. 6 for NGC 5506, and Fig. 7 for NGC 5899. We chose to show the results only for [Fe II] λ1.2570 μm, Pa βλ1.2822 μm (or Br γλ2.1661 μm in one case), and H_2λ2.1218 μm because these are the strongest emission lines allowing the mapping of the ionized gas properties via the [Fe II] and Pa β (or Br γ) emission lines, and the warm molecular gas properties through the H_2 emission line above. Although the nuclear spectra of some galaxies show further coronal lines, as [S IX] λ1.2525 μm and [Ca VIII] λ2.3211 μm, their flux distributions are unresolved or barely resolved and are not shown here, leaving a detailed discussion about these lines together with that of the gas excitation to be presented in Paper B.

In the next subsections we discuss separately the results for each map, where we have masked out pixels with bad line fits, flagged according to the following criteria, applied to all maps: (i) relative uncertainties in the line fluxes larger than 30 per cent; (ii) uncertainties in velocity and velocity dispersions larger than 50 km s^{-1}.

5.1 Flux distributions

Flux maps are shown in the first row of Figs 2–7, where we have drawn the position angle (PA) of the major axis of the galaxy as given in the HYPERLEDA data base (Prugniel et al. 2001) over the continuum images (leftmost panel) and H_2 flux and velocity maps. In all emission line maps, the peak flux is observed at the location of the continuum peak, defined as the origin of the coordinates and identified with the galaxy nucleus. The flux distributions for the selected emission lines cover most of the FOV, corresponding to maximum distances from the nucleus varying from 100 pc for NGC 3227 to 410 pc for NGC 788.

The direction of the largest extent of the [Fe II] λ1.25 μm and Pa β flux distributions follows the orientation of the ionization axis, and which in many cases approximately coincides with the orientation of the major axis of the galaxy in our sample. Exceptions are the cases of NGC 788 where they are oriented at a small angle relative to the major axis, and NGC 5506, where the largest extent of the [Fe II] emission is perpendicular to the major axis. Although also showing the highest emission levels following the major axis orientation, the H_2λ2.12 μm flux maps usually show emission more spread over all directions, being less collimated than the ionized gas emission. The only exception is NGC 788, for which the strongest H_2 emission is more extended perpendicularly to the major axis of the galaxy.

5.2 Line-ratio maps

Here we describe briefly the main features observed in the line-ratio maps; a more in-depth discussion of the gas excitation will be presented in Paper B.

The reddening and line-ratio maps are shown in the first column of Figs 2–7, below the galaxy continuum image.

The $E(B-V)$ map was obtained from

$$E(B-V) = 4.74 \log \left(\frac{5.88}{F_{\mathrm{Pa}\,\beta}/F_{\mathrm{Br}\,\gamma}} \right), \quad (1)$$

where $F_{\mathrm{Pa}\,\beta}$ and $F_{\mathrm{Br}\,\gamma}$ are the corresponding line fluxes and we have adopted in the derivation of the expression above the Cardelli, Clayton & Mathis (1989) extinction law and $F_{\mathrm{Pa}\,\beta}/F_{\mathrm{Br}\,\gamma}$ theoretical ratio of 5.88 (Osterbrock & Ferland 2006).

The $E(B-V)$ values are mostly in the range 1–3, reaching the highest values at the nucleus of NGC 5506 ($E(B-V) \approx 5$) and NGC 5899 ($E(B-V) \approx 3$) while for the other galaxies the highest values are observed outwards.

The [Fe II] λ1.2570 μm/Pa β ratio maps can be used to investigate the excitation mechanism of [Fe II] (e.g. Rodríguez-Ardila, Con-

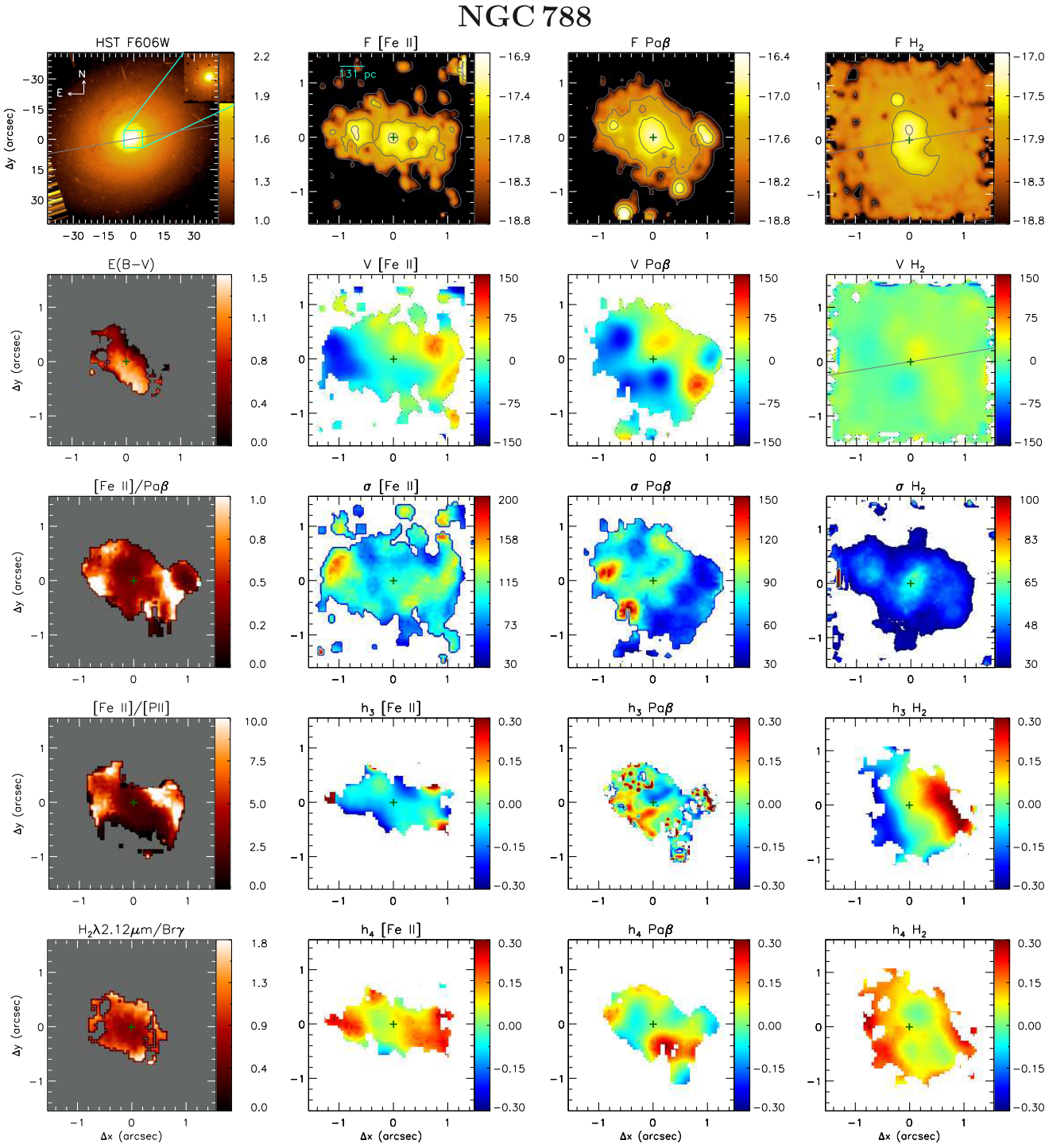

Figure 2. Maps of properties derived from the emission line profiles of NGC 788 over the Gemini NIFS FOV (3×3 arcsec^2), shown as the small cyan square over the continuum image, in the top left corner. First column, from top to bottom: *HST*-WFPC2 F606W continuum image (Malkan, Gorjian & Tam 1998) and in the insert at the top right corner the NIFS *J*-band continuum image; the grey line marks the photometric major axis; reddening $E(B-V)$ map obtained from the Pa β/Br γ line ratio; and line ratio maps identified on the top of each panel. Second column, from top to bottom: Flux F, line-of-sight velocity V_{LOS}, velocity dispersion σ, h_3 Gauss–Hermite, and h_4 Gauss–Hermite moments for the [Fe II] λ1.2570 μm emission line. Third and fourth columns: same as previous column for the Pa β and $H_2\lambda$2.1218 μm emission lines, respectively. Fluxes are shown in logarithmic units of erg s^{-1} cm^{-2}, V_{LOS} in km s^{-1}, relative to the systemic velocity of the galaxy and σ values are shown in km s^{-1}, after correction for the instrumental broadening. This galaxy is individually discussed in Section 6.1.

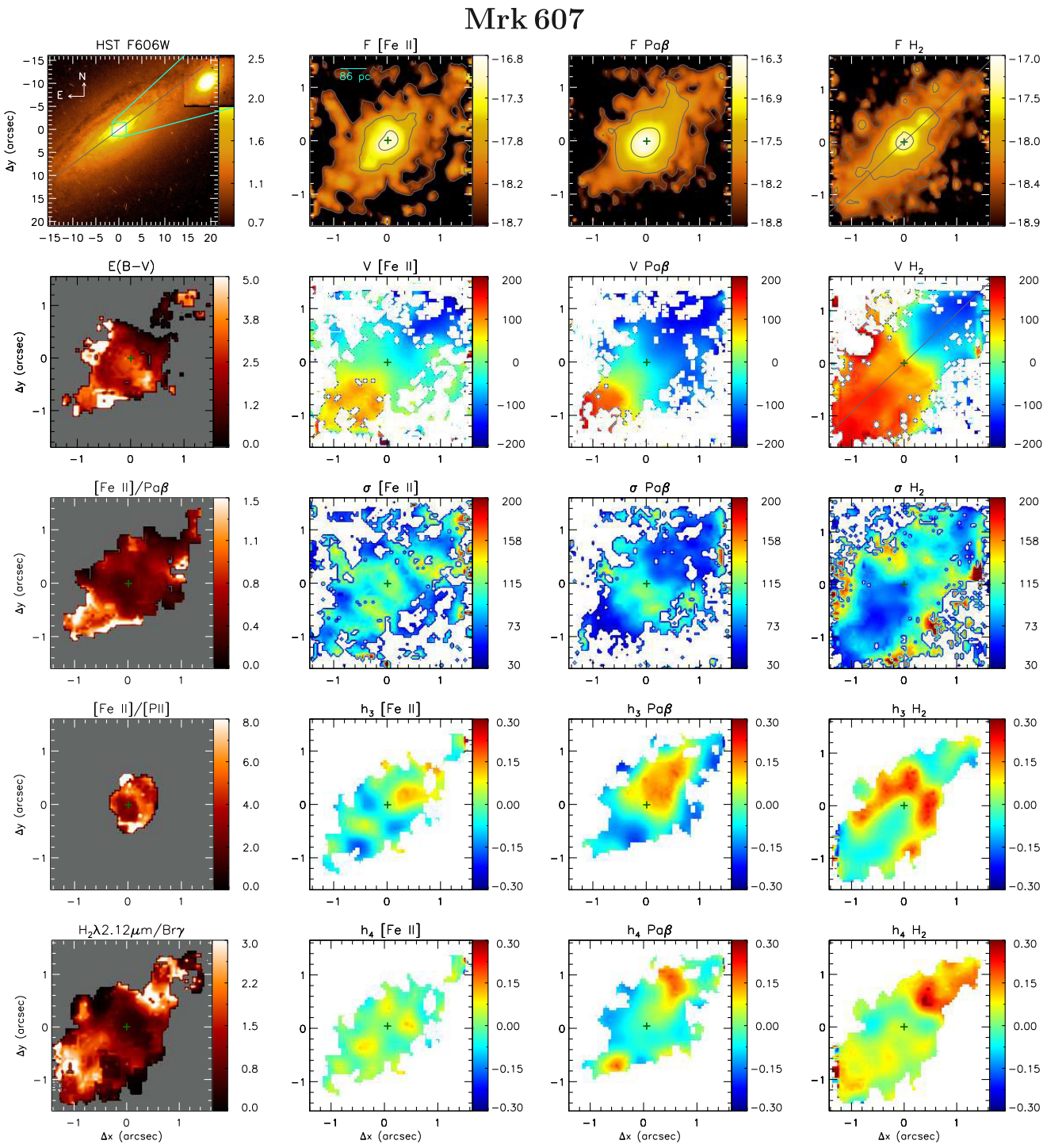

Figure 3. As in Fig. 2 for Mrk 607. This galaxy is individually discussed in Section 6.2.

tini & Viegas 2005; Riffel et al. 2008b, 2009b; Storchi-Bergmann et al. 2009), with typical values for Seyfert galaxies ranging from 0.6 to 2. Most values are observed within this range, usually increasing from the centre outwards. In the case of NGC 3227 its value increases to ≈4 in a region with the shape of an off-centred ring surrounding the nucleus in which an enhanced velocity dispersion in the [Fe II] emission lines is observed. Higher values than 2 are also observed in NGC 3516 and NGC 5899, also in association with regions of higher velocity dispersion than the surroundings, suggesting the contribution of shocks for the gas emission.

The [Fe II] λ1.2570 μm/[P II] λ1.8861 μm line ratio can also be an indicator of shocks (Storchi-Bergmann et al. 2009), if its value becomes larger than ≈2. The corresponding maps are compact, due to the small extent of the [P II] emission, with typical values of ≈5 at the nucleus and increasing to ≈10 at ≈0.″5, thus supporting the presence of shocks. In the cases of NGC 3227 and NGC 5899, the

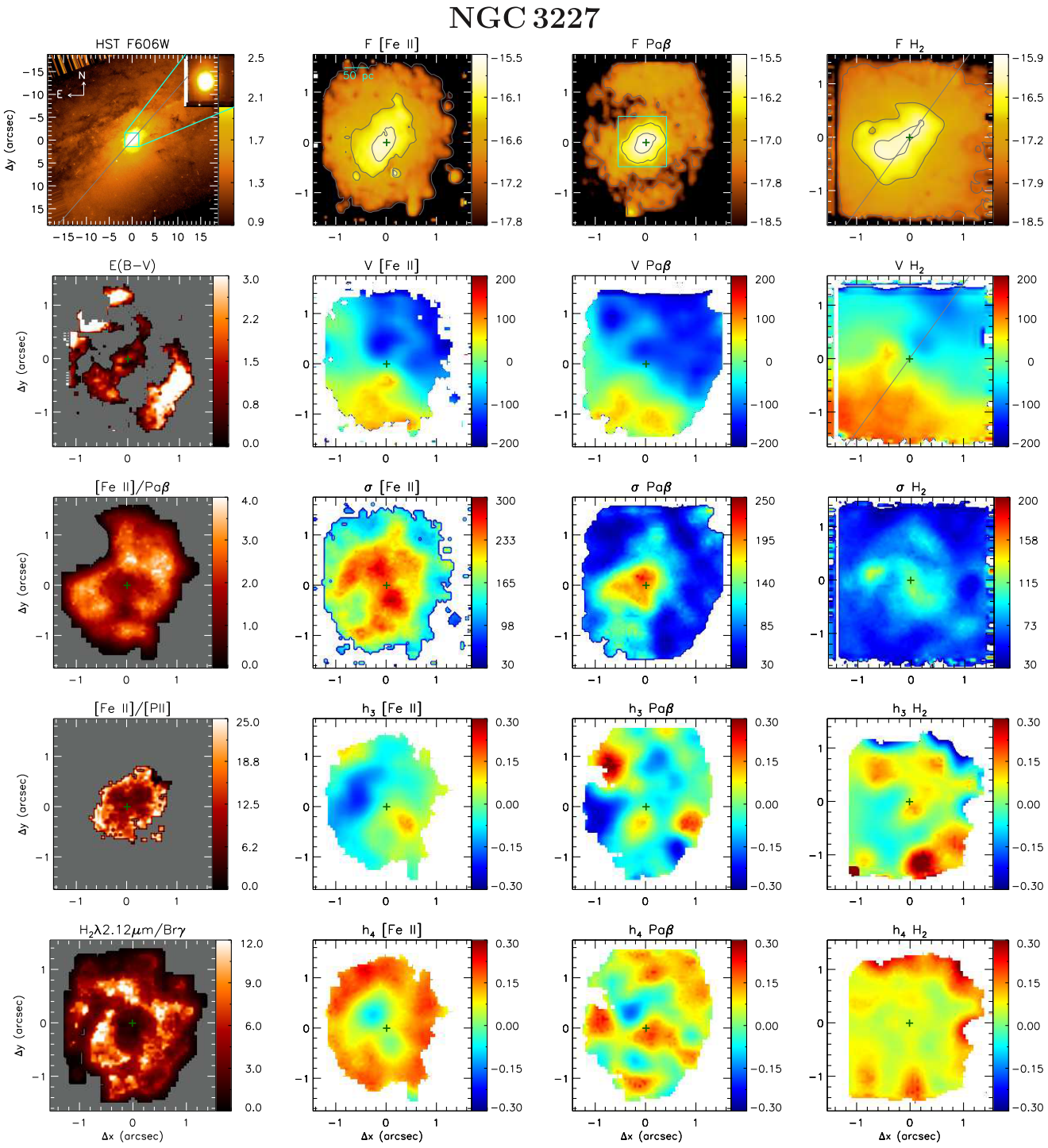

Figure 4. As in Fig. 2 for NGC 3227. The cyan square in the Pa β flux map shows the region in which we had to subtract the contribution of a broad component. This galaxy is individually discussed in Section 6.3.

off-nuclear values reach values larger than 10, also in association with high [Fe II] σ values, supporting even stronger contribution from shocks.

The H_2 λ2.1218 μm/Br γ, used to investigate the origin of the H_2 excitation, is usually in the range 0.6–2 for Seyfert galaxies (Rodríguez-Ardila et al. 2005; Riffel et al. 2008b, 2009b; Storchi-Bergmann et al. 2009). Most measured values are indeed in this range, with a general behaviour of showing the lowest ratios at the nucleus and increasing outwards, that we attribute to the destruction of the H_2 molecule by the strong radiation field close to the nucleus. The lowest values – lower than 2 – are observed for NGC 788 and NGC 5506, while the highest, reaching values in the range 8–10, are seen again in NGC 3227, NGC 3516, and NGC 5899, at similar locations as those where an enhancement is seen in [Fe II]/Pa β and [Fe II] σ values, supporting again a contribution from shocks.

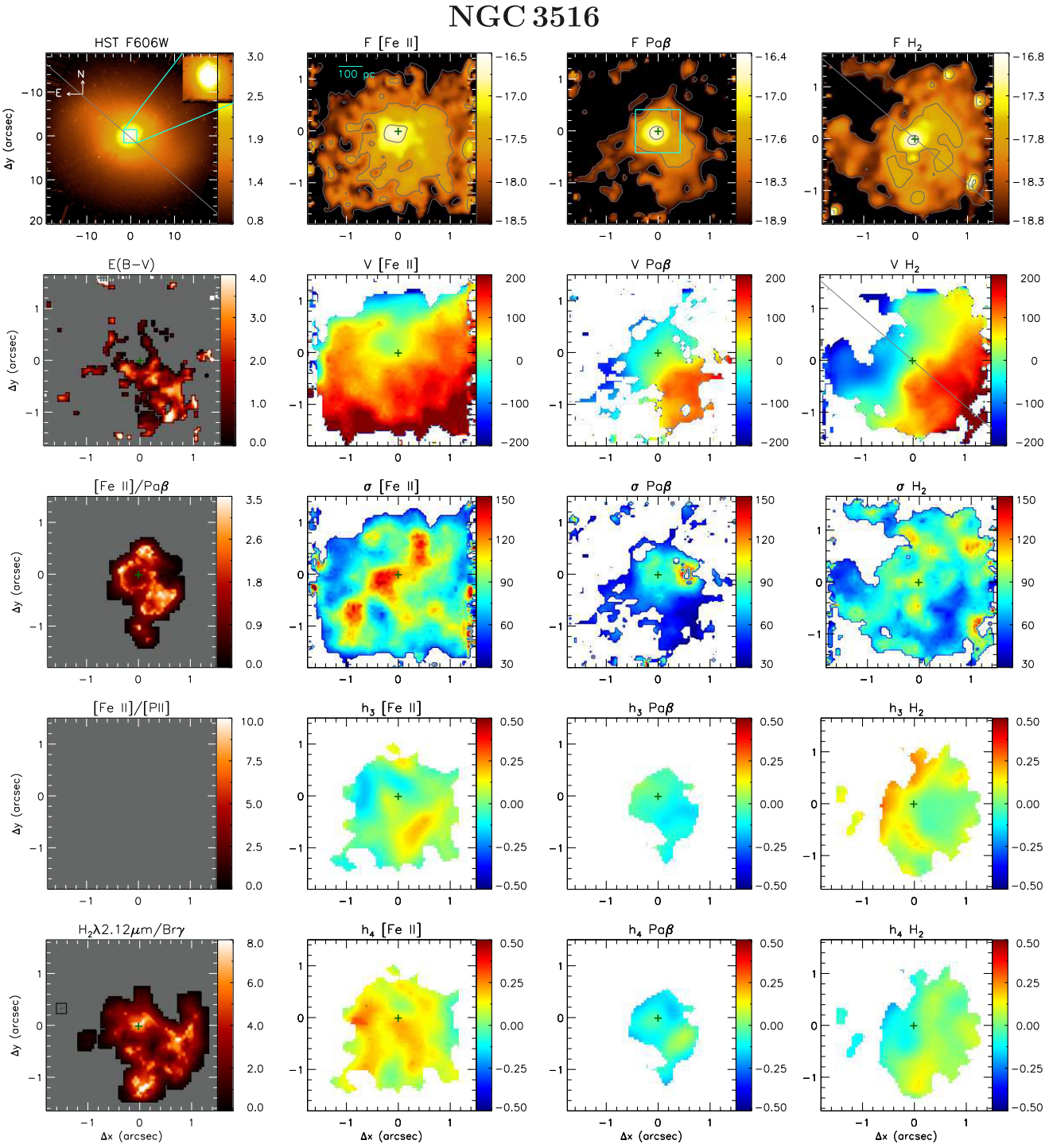

Figure 5. As in Fig. 2 for NGC 3516. The cyan square in the Pa β flux map shows the region in which we had to subtract the contribution of a broad component. This galaxy is individually discussed in Section 6.4.

5.3 Line-of-sight velocity fields

The line-of-sight velocity ($V_{\rm LOS}$) fields are shown in the second line of Figs 2–7, after the subtraction of the systemic velocity obtained through the fit of a rotating disc model to the H_2 velocity field. Again, here we just describe the general features of these velocity fields, as a proper discussion is deferred to Paper B.

The most common characteristic of the velocity fields is the rotation pattern that is clearer in the H_2 velocity maps (presenting the typical 'spider diagram' structure, Binney & Tremaine 1987). The H_2 velocity amplitudes is similar to those also seen in the [Fe II] and Pa β velocity fields, except in the case of NGC 788, for which the H_2 rotation amplitude is smaller. The rotation pattern can also be seen in the [Fe II] and Pa β velocity fields, but in these cases it is usually disturbed – more in the case of [Fe II] than in the case of Pa β – indicating the presence of additional kinematic components, usually associated with enhanced σ values.

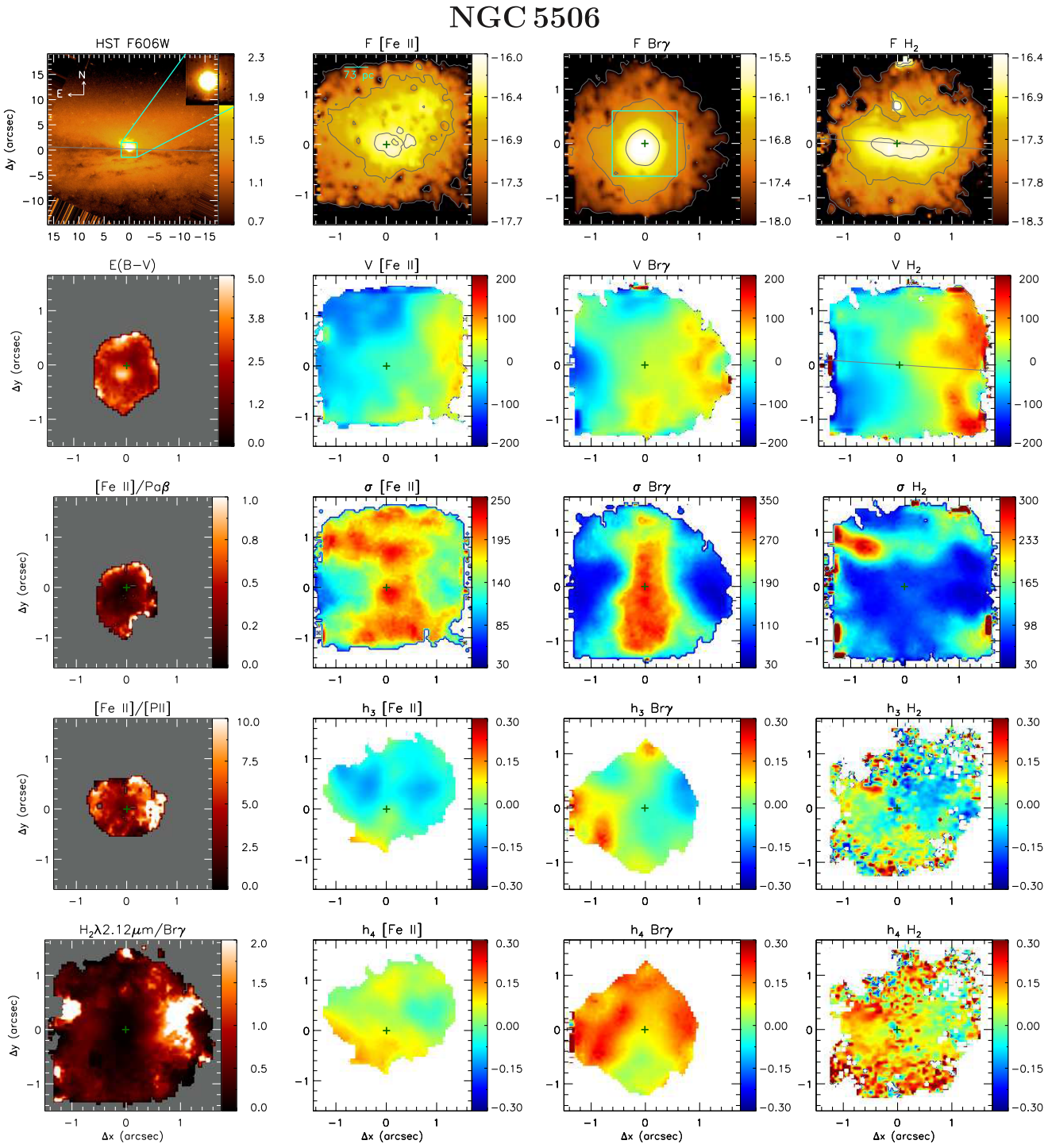

Figure 6. As in Fig. 2 for NGC 5506. The cyan square in the Pa β flux map shows the region in which we had to subtract the contribution of a broad component (although less broad than in the previous Seyfert 1 galaxies). This galaxy is individually discussed in Section 6.5.

5.4 Velocity dispersion maps

These maps are shown in the third line of Figs 2–7.

The [Fe II] σ maps usually show the highest values, reaching up to ≈150–300 km s^{-1}, while the H_2 maps show the lowest values, in the range ≈40–90 km s^{-1}. The Pa β σ maps are similar to those of [Fe II] although reaching somewhat overall lower values, in the range ≈40–250 km s^{-1}. An exception is the case of NGC 5506 that shows regions of enhanced σ to ≈350 km s^{-1} for all emission lines, extended perpendicularly to the major axis for [Fe II] and Pa β and in patches parallel to the major axis in H_2; such patches are also seen in [Fe II].

5.5 h_3 and h_4 Gauss–Hermite moments

The h_3 and h_4 maps show values ranging from –0.3 to 0.3 for all emission lines. An inverse correlation between the h_3 map and the

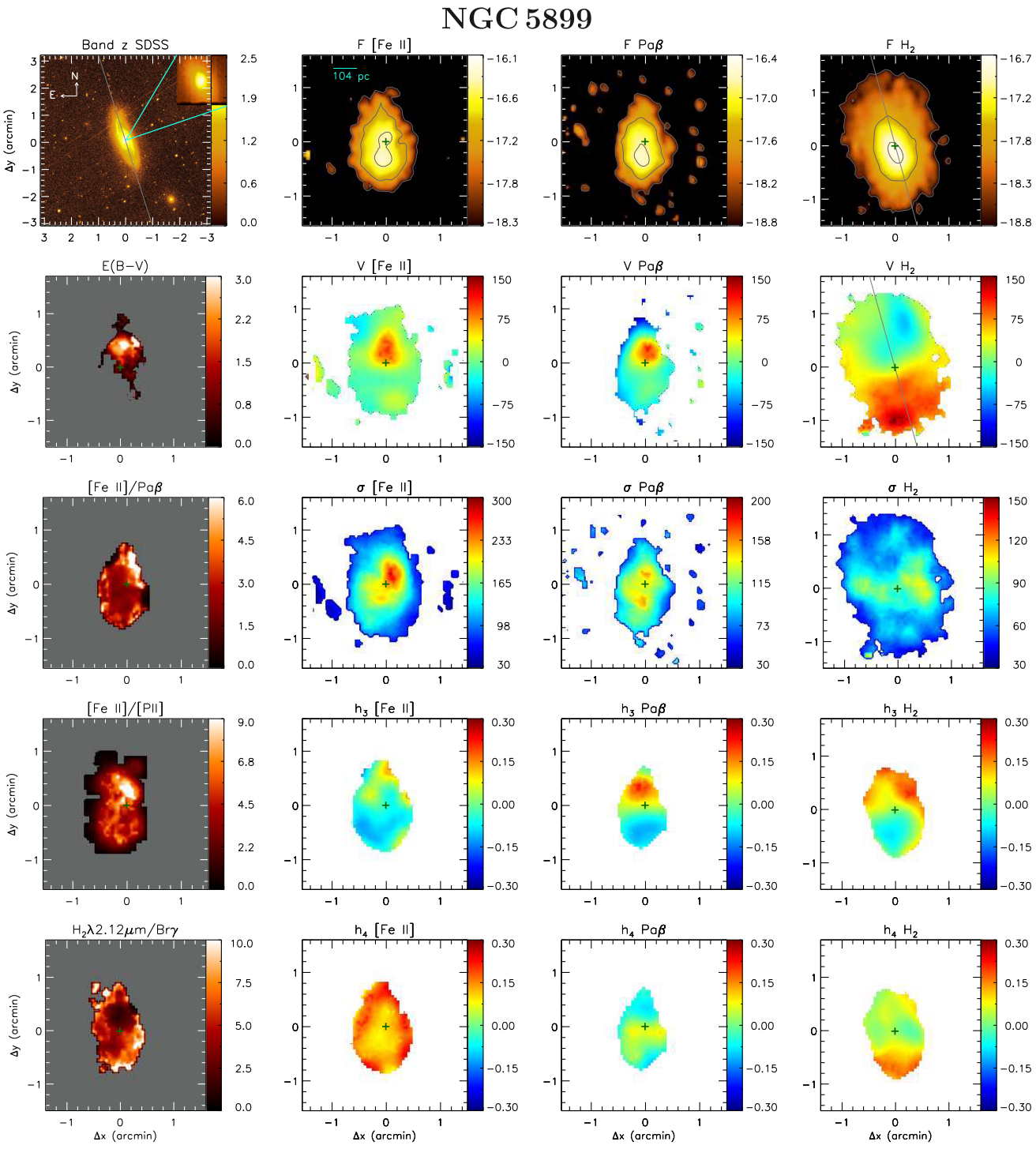

Figure 7. As in Fig. 2 for NGC 5899, but with the large-scale image from SDSS at the *z* band (Baillard et al. 2011). This galaxy is individually discussed in Section 6.6.

velocity fields is observed for all emission lines: positive values of h_3 are seen at the locations where negative velocities are observed in the velocity fields, while negative values are seen where positive velocities are observed. This means that red wings are observed in blueshifted emission lines, while blue wings are observed in redshifted emission lines.

We also observe in some cases (e.g. for the three emission lines in NGC 3227 and some of the lines in the other galaxies) an inverse correlation between the h_4 and the velocity dispersion maps. Positive values and highest values of h_4 are seen at the locations showing the lowest velocity dispersion values, while values zero or most negative ones are seen in the regions with the highest velocity dispersion.

5.6 Total gas mass and surface mass density distributions

The measurement of gas masses and surface mass densities within the inner few 100 pc of the host galaxies of AGN can be used to evaluate the gas reservoir available to trigger and maintain the nuclear activity, as well as the formation of new stars in the circumnuclear region. The presence of recent star formation in the circumnuclear region of active galaxies has been evidenced via the observation of low-stellar velocity dispersion structures (Riffel et al. 2017) and their association with young stars (e.g. Storchi-Bergmann et al. 2012). We can also use gas mass estimates in the vicinity of AGN to look for a possible correlation between the amount of available gas and the power of the AGN.

We have calculated the ionized gas masses, in units of solar masses ($M_\odot$) using the following expression (e.g. Scoville et al. 1982; Riffel et al. 2008a; Storchi-Bergmann et al. 2009; Schönell et al. 2014, 2017):

$$M_{\rm H\,II} \approx 5.1 \times 10^{16} \left(\frac{F_{\rm Pa\,\beta}}{\rm erg\,s^{-1}cm^{-2}}\right) \left(\frac{D}{\rm Mpc}\right)^2 [M_\odot], \quad (2)$$

where $F_{\rm Pa\,\beta}$ is the flux in the Pa β line and D is the distance to the galaxy.

This equation was obtained from Scoville et al. (1982) assuming an electron temperature of $T = 10^4$ K, electron density of $N_{\rm e} = 100$ cm^{-3}, and case B recombination (Osterbrock & Ferland 2006) values applicable to the inner kiloparsec of active galaxies. The flux of Br γ used in the original equation was replaced by the stronger Pa β one assuming the theoretical ratio $F_{\rm Pa\,\beta}/F_{\rm Br\,\gamma} = 5.88$ (Osterbrock & Ferland 2006). For NGC 5506, we did use the flux of Br γ emission line instead of Pa β, as the signal to noise in the *J*-band spectrum is worse than in the *K*-band one, particularly in the extranuclear regions.

The mass of the warm molecular gas (in $M_\odot$) was obtained using (Scoville et al. 1982):

$$M_{\rm H_2} \approx 5.0776 \times 10^{13} \left(\frac{F_{\rm H_2\lambda 2.1218}}{\rm erg\,s^{-1}cm^{-2}}\right) \left(\frac{D}{\rm Mpc}\right)^2 [M_\odot], \quad (3)$$

where $F_{\rm H_2\lambda 2.1218}$ is the flux for the corresponding emission line.

In the derivation of the above equation by Scoville et al. (1982) it was assumed that the vibrational temperature is $T = 2000$ K, indicating a thermalized gas which is valid for $n_{\rm H_2} > 10^{4.5}$ cm^{-3}. Previous studies by members of our group have found that the assumption of thermal equilibrium is indeed applicable for nearby AGNs and the derived temperatures are very close to the above value (Storchi-Bergmann et al. 2009; Diniz et al. 2015).

Uncertainties in the derived mass values were obtained considering that the mass derived from both equations (2) and (3) are directly proportional to the line fluxes. All the mass uncertainties are thus lower than 30 per cent, as we have masked out regions with flux uncertainties larger than this value. The actual uncertainties may be somewhat higher due to further uncertainties in the absolute flux calibration. In addition, we cannot derive precise physical parameters such as gas density and temperature, thus, we have to rely on the above assumptions even though they are just 'educated estimates' based on our previous similar studies.

We show the surface mass density Σ distributions of ionized and warm molecular gas – $\Sigma_{\rm H\,II}$ and $\Sigma_{\rm H_2}$, respectively – in the first two columns of panels of Fig. 8, and the corresponding azimuthally averaged profiles in the third column, in units of solar masses per parsec square. The surface mass densities were obtained by calculating the gas masses in each spaxel using the equations above and dividing them by the surface area of each spaxel, taking into account projection effects via the use of the disc inclinations quoted in Riffel et al. (2018). The resulting ionized gas surface mass density distributions are in some cases more compact when compared with that of the warm molecular gas, that seems to extend farther and more uniformly from the nucleus than the ionized gas.

The azimuthally averaged profiles of $\Sigma_{\rm H\,II}$ and $\Sigma_{\rm H_2}$, shown in the last column of Fig. 8, reveal that typical ratios between the two surface mass densities within the inner ≈100 pc are of the order of 10^3 and that Σ gradients are steeper for the ionized than for the molecular gas.

In Table 3 we show the integrated gas mass values (for the whole FOV) as well as the average surface mass densities (in units of $M_\odot$ pc^{-2}) obtained as the ratio between the integrated masses and the area over which they are distributed, listed also in the Table. We also include in Table 3 an estimate of the cold molecular gas mass. A number of studies have derived the ratio between the cold and warm H_2 gas masses by comparing the masses obtained using the cold CO molecular lines observed in millimetric wavelengths with that of the warm H_2 observed in the near-IR. Dale et al. (2005) obtained ratios in the range 10^5–10^7, while Müller Sánchez et al. (2006), using a larger sample of 16 luminous and ultraluminous infrared galaxies, derived a ratio $M_{\rm cold}/M_{\rm warm} = 1$–$5 \times 10^6$. More recently, Mazzalay et al. (2013) compiled from the literature values of $M_{\rm cold}$ derived from CO observations and H_2(2.12 μm) luminosities for a larger number of galaxies, covering a wider range of luminosities, morphological, and nuclear activity types. From those data, they propose that an estimate of the cold H_2 gas mass can be obtained from the flux of the warm $H_2\lambda$2.1218 line as

$$M_{\rm H_2\,cold} \approx 1174 \left(\frac{L_{\rm H_2\lambda 2.1218}}{L_\odot}\right), \quad (4)$$

where $L_{\rm H_2\lambda 2.1218}$ is the luminosity of the H_2(2.12 μm) line. The error associated with the factor $\beta = 1174$ is ≈35 per cent, according to Mazzalay et al. (2013).

Table 3 shows that the integrated mass of warm H_2 gas (within typically 100–400 pc from the nucleus) ranges from 106 $M_\odot$ for Mrk 607 to 820 $M_\odot$ for NGC 5506, while the estimated mass of cold molecular gas ranges from 8×10^7 $M_\odot$ for Mrk 607 to 6×10^8 $M_\odot$ for NGC 5506. The masses of ionized gas range from 1.8×10^5 $M_\odot$ for NGC 3516 to 1.9×10^7 $M_\odot$ for NGC 5506. We point out again that the uncertainties in the calculated masses, presented in Table 3, were obtained only by propagating the line flux uncertainties and are thus lower limits, considering that there are additional uncertainties in adopted physical properties – e.g. on the $M_{\rm H_2\,cold}/M_{\rm H_2}$ ratio, H_2 vibrational temperatures, and electron densities.

6 DISCUSSION

In this section we discuss individually each galaxy presenting a brief review of previous results from the literature, trying to relate them with ours. We also discuss and analyse the masses of ionized and molecular gas, as well as their surface mass density distributions and the global properties of the gas kinematics, leaving the kinematic modelling and the analysis of the gas kinematics and excitation to Paper B.

6.1 NGC 788

NGC 788 (Fig. 2) was identified as a Seyfert galaxy by Huchra, Wyatt & Davis (1982), and has been observed in the optical (Hamuy & Maza 1987; Wagner 1988; Cruz-Gonzalez et al. 1994; Kay 1994), radio (Ulvestad & Wilson 1989), and millimetre (Heckman et al.

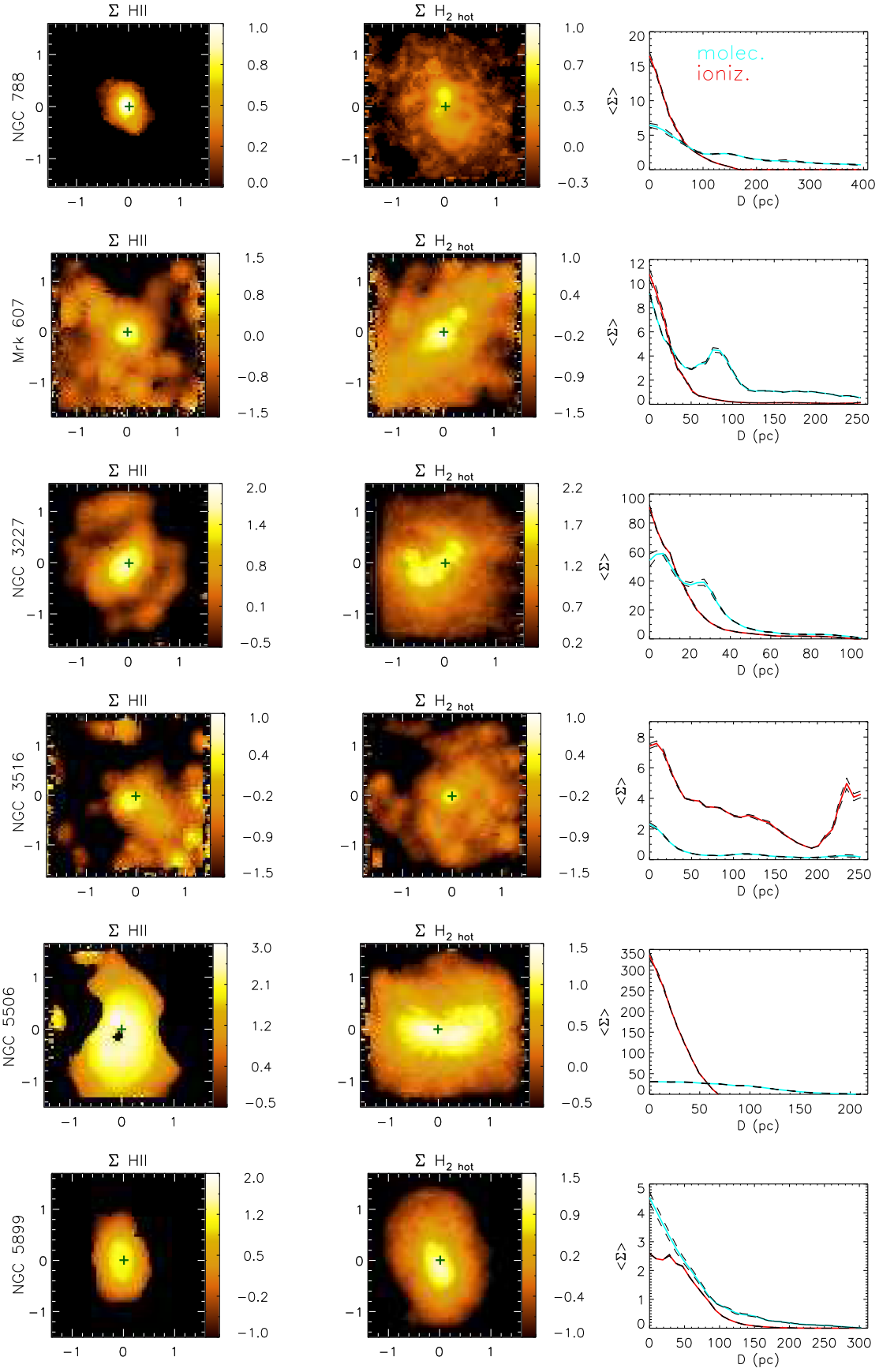

Figure 8. Surface gas mass density distributions Σ: in the first column we show $\Sigma_{\rm H\,II}$ in units of $M_\odot$ pc^{-2}); in the second column $\Sigma_{\rm H_2}$ in units of 10^{-3} $M_\odot$ pc^{-2}, and in the third the corresponding azimuthally averaged gradients, showing more centrally peaked distributions for the ionized gas.

Table 3. Areas, masses, and average surface mass density Σ values for the ionized, warm, and estimated cold molecular gas within the Gemini NIFS FOV.

Galaxies	Area (H_2) 10^5 pc^2	Area (H II) 10^5 pc^2	M $(H_2)_{hot}$ 10^2 M$_\odot$	M $(H_2)_{cold}$ 10^7 M$_\odot$	M (H II) 10^5 M$_\odot$	Σ $(H_2)_{hot}$ 10^{-3} M$_\odot$ pc^{-2}	Σ $(H_2)_{cold}$ 10^3 M$_\odot$ pc^{-2}	Σ (H II) M$_\odot$ pc^{-2}
NGC 788	6.2	5.5	5.9 ± 0.15	43 ± 1	28 ± 9.8	0.9 ± 0.03	0.8 ± 0.02	5.2 ± 1.8
Mrk 607	0.6	0.2	1.1 ± 0.2	8 ± 1	6.4 ± 4.9	1.8 ± 0.3	3.3 ± 0.6	28.0 ± 22.0
NGC 3227	0.9	0.4	7.5 ± 0.4	54 ± 3	10.0 ± 1.0	8.0 ± 0.4	12.0 ± 0.6	23.0 ± 2.0
NGC 3516	0.8	0.6	3.0 ± 1.7	22 ± 12	1.8 ± 1.0	3.7 ± 2.0	3.6 ± 2.0	2.9 ± 1.6
NGC 5506	1.4	1.2	8.2 ± 0.4	60 ± 3	190.0 ± 10.0	5.7 ± 0.3	4.6 ± 0.2	140.0 ± 7.0
NGC 5899	1.9	0.9	3.3 ± 0.3	23 ± 2	2.5 ± 1.8	1.7 ± 0.2	2.7 ± 0.2	2.8 ± 2.0

1989) wavebands. This galaxy is an early-type spiral with faint arms visible up to ≈30″ from the nucleus (Evans et al. 1996), most conspicuous to the north-west of the nucleus with a string of bright compact H II regions, while a complex of fainter H II regions is associated with a southern arm (Evans et al. 1996).

The kinematics major axis PA ≈ 125° was determined from the V_{LOS} fields (Fig. 2), with a value close to that obtained by Riffel et al. (2017) for the stellar kinematics of ≈ 130°. The velocity amplitude observed for [Fe II] and Pa β, of ≈150 km s^{-1} is much higher than that for H_2, of only ≈50 km s^{-1}. These higher velocities are associated with a more collimated emission and higher velocity dispersions suggesting the presence of a bipolar outflow along the east–west direction, as suggested from the morphology of the gas emission in the [Fe II] flux map.

The $E(B-V)$ map from Fig. 2 has the highest values to south-west of the nucleus, which coincide with a dust lane seen in the *HST* - F606W optical continuum image from Martini et al. (2003).

6.2 Mrk 607

Mrk 607 (Fig. 3) is an Sa galaxy hosting a Seyfert 2 nucleus. A continuum image from Ferruit, Wilson & Mulchaey (2000) shows a high ellipticity of ≈0.60, yielding an inclination $i \approx 67°$), with major axis PA of −43°, which agrees with our estimate of the kinematic major axis orientation of ≈−38° from the H_2 velocity field (Paper B).

Our data reveal that the three velocity fields – [Fe II], Pa β, and H_2 – show what seems to be a rotation pattern, very steep in the centre in H_2 and less steep in the first two lines. Spiral dust lanes are clearly visible in the *HST* F547 continuum image of the inner 8 arcsec (1.4 kpc) (Ferruit et al. 2000). The high inclination of the galaxy may explain the large velocity dispersions observed. In the central 5 arcsec (875 pc) it presents weak radio emission extended along PA ≈ 180° (Colbert et al. 1996; Nagar et al. 1999) which is not aligned with the axis of the most extended gas emission, which is observed along the galaxy major axis.

The $E(B-V)$ map from Fig. 3 has high values (≈5) to south-east/west of the nucleus, which coincide with a dust lane seen in the *HST* - F606W optical continuum image from Martini et al. (2003).

6.3 NGC 3227

NGC 3227 (Fig. 4) is a well-studied barred galaxy, with a Seyfert 1.5 nucleus (Ho, Filippenko & Sargent 1997) and in interaction with the dwarf elliptical galaxy NGC 3226 (Mundell et al. 2004). The galactic disc has an inclination of 56°, with an outer photometric major axis at a position angle PA = 158° (Mundell et al. 1995). This value agrees with the PA ≈ 155° we have obtained from the fit of the H_2 V_{LOS} velocity field (Paper B), and with the value of 156° found by Riffel et al. (2017) from the stellar kinematics. The three emission line velocity fields show a rotation pattern, that is nevertheless distorted due to the presence of additional components, mainly to the north-east, east, and south-east. These components are most conspicuous in [Fe II] and Pa β velocity maps and are associated with regions of enhanced velocity dispersion.

The central region has been mapped in ^{12}CO(1-0) and ^{12}CO(2-1) by Schinnerer, Eckart & Tacconi (2000), who detected molecular gas very close to the nucleus (within ≈13 pc), in agreement with our results that show a large molecular gas concentration towards the centre (see the surface mass density profile in the third line of Fig. 8). In addition, Schinnerer et al. (2000) found an asymmetric nuclear ring with a diameter of about 3″.0 (220 pc), which seems to correspond to the structure delineated in the line ratio maps [Fe II]/Pa β and H_2/Br γ of Fig. 4.

The inner kiloparsec hosts a radio jet at PA ≈−10° and a conical NLR outflow at PA ≈ 15° (Mundell et al. 1995), while Arribas & Mediavilla (1994) report an H α outflow at PA ≈ 50°. The extent of the [Fe II] emission to the north, as well as its enhanced velocity dispersion may be related to the radio emission, while the outflows observed at PAs between 15° and 50° can explain the deviation from rotation observed in the velocity fields of [Fe II] and Pa β to the north-east. Signatures of gas outflows in NGC 3227 have also been observed by Davies et al. (2014) in the inner 1–2 arcsec using near-IR IFS observations with the instrument SINFONI at the VLT. A *V–H* colour map shows dust lanes to the south-west of the nucleus (Martini et al. 2003; Davies et al. 2014), which are cospatial with the highest $E(B-V)$ values seen in Fig. 4.

6.4 NGC 3516

The Seyfert 1 nucleus of this SB0 galaxy (Fig. 5) shows variable ultraviolet absorption lines (Voit, Shull & Begelman 1987; Kriss et al. 1996) as well as variable broad emission lines and continuum (Koratkar et al. 1996). Spectroscopic studies of the gaseous kinematics using either long-slit (Ulrich & Pequignot 1980; Goad & Gallagher 1987, 1988; Mulchaey et al. 1992) or integral field spectroscopy (Veilleux, Tully & Bland-Hawthorn 1993; Aoki et al. 1994; Arribas & Mediavilla 1994) have outlined multiple spectral components displaying strong deviations from 'normal' galaxy rotation. Two general models have been proposed to explain the morphology and the kinematics of the emission line gas that presents a Z-shaped structure covering the inner 5″.0: a bent bipolar mass outflow, first suggested by Goad & Gallagher (1987) and further developed by Mulchaey et al. (1992) and Veilleux et al. (1993), and a precessing twin-jet model by Veilleux et al. (1993). The stellar rotation curve obtained by Arribas et al. (1997) yields a systemic velocity of 2593 ± 15 km s^{-1}, close to that derived by Riffel et al. (2017) of ≈2631 km s^{-1}. The kinematic major axis obtained by Arribas et al. (1997) has PA = 53° ± 5° and is consistent with our results for the stellar kinematics (Riffel et al. 2017) and also

with the orientation of the kinematic major axis of the molecular gas of ≈60°.

6.5 NGC 5506

The nucleus of NGC 5506 (Fig. 6) is classified as an Sy1.9 based on the detection of broad wings in the Pa β profile (Blanco, Ward & Wright 1990). However, more recently, Nagar et al. (2002) presented evidence that NGC 5506 is an obscured narrow-line Sy1, via the detection of the permitted O Iλ1.129 μm line, together with a broad pedestal of Pa β and rapid X-ray variability. The galaxy nucleus is very compact in the mid-IR, with an apparent optical depth of $\tau^{\rm app}_{10\,\mu\rm m} \approx 1.4$ (Roche et al. 1991, 2007; Siebenmorgen, Krügel & Spoon 2004), although NGC 5506 also shows variations in its silicate absorption depth on parsec scales (Roche et al. 2007). The optical spectrum has strong [O III] and [N II] narrow lines (Zaw, Farrar & Greene 2009). The log([O III]/H β) and log([N II]/H α) line ratios, 0.88 and −0.09, respectively (Kewley et al. 2001), place it firmly in the Seyfert region of the BPT (Baldwin, Phillips & Telervich) diagram.

NGC 5506 is close to edge-on, with an inclination of 75°, above and below which ionized gas is in outflow within cones with an opening angle of ≈80° (Maiolino et al. 1994). These outflows are consistent with the distribution of enhanced sigma values we observe in the ionized gas in a vertical structure crossing the galaxy plane and opening to the north and south of it (Fig. 6). The outflow to the north is also well traced by the [Fe II] flux distribution (its highest emission shows an approximately conical shape), while the H_2 flux distribution seems to better trace the gas in the galaxy plane, as it is oriented along this direction.

As observed in Fig. 1, the nucleus of NGC 5506 shows a steep red continuum over the 2.1–2.4 μm spectral range that can be attributed to a blackbody source with temperature ≈1000 K. Although large-scale dust is observed in the central region of this galaxy, possibly due to its high inclination and as seen in the *V–H* dust map from Martini et al. (2003), the origin of the *K*-band continuum is most probably hot dust emission from the AGN torus, as already observed for other active galaxies (e.g. Riffel, Storchi-Bergmann & McGregor 2009c; Burtscher et al. 2015; Diniz, Riffel & Dors 2018).

6.6 NGC 5899

This inclined SAB(rs)c galaxy (Fig. 7) is reported to be in a pair and presents an optical Seyfert 2 spectrum (de Vaucouleurs et al. 1991). The stellar kinematics derived by Riffel et al. (2017) gives a PA ≈ 24°, that is somewhat distinct from that obtained by us for the molecular gas (Paper B), of ≈4°. The kinematics of the ionized gas is very different from that of the molecular gas (Fig. 7): while the latter seems to be dominated by rotation in the inclined galaxy plane, with blueshifts to the north and redshifts to the south, the ionized gas kinematics shows velocities that are opposite to that observed in the H_2 velocity field. A possible interpretation is that the ionized gas is tracing an outflow at PA ≈ 0°, as supported also by the north–south elongation observed mostly in the [Fe II] flux map and by the enhanced velocity dispersion observed at these locations.

6.7 Global properties

6.7.1 Surface mass density distributions

Fig. 8 shows that the molecular gas seems to be more evenly distributed over the field of view than the ionized gas, which is more concentrated towards the nucleus and shows a more patchy and sometimes collimated mass distribution. The more peaked distribution of the ionized gas is clearly seen in the average surface mass density profiles shown in the third column of Fig. 8 for the galaxies NGC 788, Mrk 607, NGC 3227, and NGC 5506. In the cases of NGC 3516 and NGC 5899, the average profiles of the molecular and ionized gas surface mass densities are similar to each other. The prevalence of more concentrated ionized gas profiles than those in H_2 can be attributed to the fact that the neutral gas rapidly absorbs the ionizing photons from the AGN, thus concentrating in its vicinity and/or along the ionization axis – the preferred direction of escape of the AGN radiation.

The H_2, on the other hand, has another source of excitation, as shown in our previous works (e.g. Ilha, Bianchin & Riffel 2016), where the typical temperature is ≈2000 K and the line ratios suggest thermal excitation. The heating to excite the rotational and vibrational modes of the H_2 molecule can be attributed to X-rays originating in the AGN. These X-rays penetrate deep along the galaxy plane in every direction heating the region and exciting the H_2 molecule. In addition, in the regions closest to the AGN, where the temperature can reach ∼15 000 K, the H_2 molecules are destroyed, and we only see those more deeply embedded in the circumnuclear dust, where they are shielded from the strongest AGN radiation.

We thus conclude that the distinct nature of the excitation of the ionized and the molecular gas and different physical conditions of the regions where they originate can explain the difference in the gas surface mass density profiles.

6.7.2 Gas kinematics

In this section we discuss briefly the global properties of the gas kinematics, with the goal of just highlighting apparent correlations among properties and differences between the molecular and ionized gas kinematics. As we already pointed out, we will leave the modelling of the velocity fields, the quantification of possible inflows and outflows, as well as the determination of the impact of the outflows on the host galaxy (feedback) to Paper B.

A global property of the gas kinematics, as seen in Figs 2–7, is that the warm H_2 velocity field is dominated by rotation in the plane of the galaxy. Although the ionized gas velocity fields show also signatures of rotation, the rotation pattern is distorted due to the presence of additional components that can be attributed to outflows and which are usually associated with an increase in the velocity dispersion.

The above results are in agreement with those of previous studies by our AGNIFS group, in which we have additionally reported, for H_2, the presence of inflows in a number of galaxies. We have also found that outflows are most easily seen in the ionized gas (Storchi-Bergmann & Schnorr-Müller 2019) and that this gas shows a more centrally concentrated flux distribution than that of H_2 Riffel et al. (2018), also in agreement with what we found in this paper.

The most frequent presence of outflows in the ionized gas than in the molecular gas can be understood as due to the fact that the ionized gas is mostly concentrated along the ionization axis, where it can be easily pushed by an AGN outflow. The molecular gas, on the other hand, is usually destroyed by the hard AGN radiation at these locations. Thus, although the H_2 flux distributions appear also surrounding the nucleus, it is not cospatial with the ionized gas, as it originates in gas at temperatures much lower (2000 K) than those characteristic of the ionized gas (10 000 K). This is also supported

by the lower velocity dispersion of H_2. Clear examples are the cases of NGC 4151 (Storchi-Bergmann et al. 2009) and NGC 1068 (Barbosa et al. 2014) that show H_2 flux distributions surrounding the nucleus but avoiding the ionization axis. On the other hand, molecular gas outflows are observed in a number of cases, and in distant AGN hosts (Emonts et al. 2017). A possibility in these cases is that a nuclear outflow can push the surrounding gas including the H_2 gas which may be shielded from the ionizing radiation by dust, for example. We hope to revisit this point in Paper B.

Regarding the presence of outflows, we have found signatures of them in most galaxies of our sample, most clearly observed in the [Fe II] kinematics: (1) in NGC 788, along the east–west direction; (2) in NGC 3227, towards the north-east, as suggested by distortions in the velocity field and patterns in h_3 and h_4; (3) in NGC 3516, from the south-east to the north-west, as suggested by the disturbed velocity field and enhanced velocity dispersion; (4) in NGC 5506, along north–south, as suggested by the enhanced velocity dispersions; (5) and in NGC 5899, towards north and south, as indicated by the opposite velocity field between the ionized and molecular gas.

Another global property of the sample is the fact that the h_3 Gauss–Hermite moment shows an inverse correlation with the V_{LOS} in a number of cases: (1) in the Pa β line for NGC 788; (2) in Pa β and [Fe II] for Mrk 607; (3) in Pa β and H_2 in NGC 3227; (4) in Pa β and H_2 for NGC 3516; (5) in Br γ and H_2 in NGC 5506; (6) in H_2 in NGC 5899. This means that there are red wings in centrally blueshifted profiles and blue wings in redshifted ones. One possible explanation is the effect known as 'asymmetric drift' (Westfall et al. 2007): gas rotating in the galaxy plane gives origin to the 'main' velocity field – corresponding to the emission line peaks, while tenuous gas at higher latitudes rotating with lower velocity – thus lagging behind the rotation in the plane – gives origin to the wings of the profiles.

We also observe in some cases, an inverse correlation between the h_4 and the σ values – mostly positive h_4 values at the locations with low σ, and only a few negative values at locations with high σ. This has been observed in: (1) H_2 for NGC 788; (2) in the three emission lines for NGC 3227; (3) in Pa β and H_2 for NGC 3516; (4) in Br γ for NGC 5506; (5) in the three emission lines for NGC 5899.

Positive h_4 values indicate profiles more 'peaky' than a Gaussian curve, but with broader wings, while negative values indicate profiles less peaky and with less extended wings than a Gaussian. We tentatively interpret the positive h_4 values as being mostly due to the emission of gas rotating in the disc, with low σ values, while the wings could originate in diffuse gas emission, that may extend to high latitudes, increasing the range of velocities probed by the emission. The high σ and negative h_4 values are rarer, and could arise in spatially unresolved double components, and may be related to the presence of an outflow, as seems to be the case for the [Fe II] line in NGC 3227, for example (Fig. 4).

6.7.3 *Total gas masses and implied star formation rates*

In order to evaluate if the gas reservoirs accumulated in the inner few 100 pc of these galaxies have enough mass to feed the AGN, we first estimate the AGN accretion rates $\dot{m}$ using:

$$\dot{m} = \frac{L_{\rm bol}}{c^2 \eta}, \tag{5}$$

where $L_{\rm bol}$ is the bolometric luminosity of the AGN, c is the light speed, and η is the conversion efficiency of rest mass of the accreted material into radiation, that we have adopted as $\eta = 0.1$. The bolometric luminosities were determined by Riffel et al. (2018) based on the hard X-ray luminosities. The only exception is the case of Mrk 607, for which the [O III] luminosity was used instead, adopting a bolometric correction factor of 3500 (Heckman et al. 2004). The resulting accretion rates are presented in Table 4.

Table 4. Mass accretion rates $\dot{m}$, average SFR surface densities $\Sigma_{\rm SFR}$, and total SFRs.

Galaxy	$\dot{m}$ $10^{-3}\,M_\odot\,yr^{-1}$	$<\Sigma_{\rm SFR}>$ $10^{-3}\,M_\odot\,yr^{-1}kpc^{-2}$	SFR $10^{-3}\,M_\odot\,yr^{-1}$
NGC 788	49.2	2.5 ± 1.2	1.4 ± 0.7
Mrk607	0.1	26.5 ± 29.2	0.6 ± 0.7
NGC 3227	4.1	20.1 ± 2.5	0.9 ± 0.2
NGC 3516	27.9	1.1 ± 0.8	0.1 ± 0.1
NGC 5506	37.0	260 ± 18.0	31.2 ± 2.2
NGC 5899	2.4	1.0 ± 1.0	0.2 ± 0.2

As the estimated mass accretion rates to the AGN are in the range $0.1-50\times10^{-3}\,M_\odot\,yr^{-1}$, considering an AGN activity cycle of 10^7–10^8 yr, and assuming that most of the ionized and molecular gas are concentrated within the inner few 100 pc of the galaxies (Fig. 8), it can be concluded that the ionized gas mass alone would be enough to feed the AGN. Nevertheless, Table 3 shows that the estimated masses of the cold molecular gas are larger, and range from 10^7 to 10^8 $M_\odot$; therefore, there seems to be at least $\approx10^2$ times more gaseous mass in the inner few 100 pc of these galaxies than that necessary to feed the AGN.

The fate of the gas that is not used to feed the AGN can: (1) be consumed by star formation; (2) be pushed away by AGN feedback; (3) be pushed away by stellar feedback (e.g. Hopkins et al. 2016). Most probably more than one process will occur.

Here we will discuss only the possibility that the gas accumulated in the nuclear region will lead to the formation of new stars, thus calculating the star formation rate (SFR) in the inner few 100 pc. The feedback due to the observed outflows and possibility of stellar feedback will be discussed in Paper B.

Schmidt (1959) has shown that the SFR is directly related to the gas density, and later Kennicutt (1998) proposed a relation between the SFR surface density $\Sigma_{\rm SFR}$ and the ionized gas mass surface density $\Sigma_{\rm H\,II}$, as follows:

$$\frac{\Sigma_{\rm SFR}}{M_\odot\,yr^{-1}\,kpc^{-2}} = (2.5\pm0.7)\times10^{-4}\left(\frac{\Sigma_{\rm H\,II}}{M_\odot pc^{-2}}\right)^{1.4}, \tag{6}$$

Using the relation above, we obtain the mean values for $\Sigma_{\rm SFR}$ listed in Table 4, which range from 1×10^{-3} to $0.26\,M_\odot\,yr^{-1}\,kpc^{-2}$. Using the areas quoted in Table 3 for the regions occupied by the ionized gas we estimate total SFRs for the area covered by our observations (radius of $\approx$300 pc) in the range 10^{-4}–10^{-2} $M_\odot\,yr^{-1}$ (Table 3). These values are within the range of values observed for the inner few 100 pc of galaxies and circumnuclear star-forming regions (Shi, Gu & Peng 2006; Dors et al. 2008; Falcón-Barroso et al. 2014; Tsai & Hwang 2015; Riffel et al. 2016).

We therefore conclude that the mass reservoirs in the inner 300 pc of the sample galaxies can not only power the central AGN but also form new stars at low SFR ($\leq10^{-2}$ $M_\odot\,yr^{-1}$). The presence of recently formed stars in the inner few 100 pc of AGN is supported by the observation of low-stellar velocity dispersion (σ_*) structures in 10 of 16 galaxies of our sample for which we could measure σ_* (Riffel et al. 2017).

7 CONCLUSIONS

We have mapped the ionized and molecular gas flux distributions, excitation and kinematics in the inner kpc of six nearby active galaxies using AO assisted NIR *J*- and *K*-band IFS obtained with the Gemini NIFS instrument. The main conclusions of this work are listed below.

(i) The flux distributions are usually distinct for the ionized and molecular gas: while the former is more concentrated and sometimes collimated along a preferred axis, the latter is distributed more uniformly over the galaxy plane. These flux distributions lead to azimuthally averaged surface mass density profiles steeper for the ionized gas than for the molecular gas. We attribute this difference to the different excitation mechanisms: while the ionized gas is excited by the AGN radiation in regions with temperatures of about 10 000 K, close to the AGN, the molecular gas is thermally excited in regions of lower temperatures of about 2000 K, that extend farther from the nucleus;

(ii) The gas kinematics is also distinct: while the molecular gas is mostly rotating in the galaxy plane with low velocity dispersions, the ionized gas frequently shows other components associated with higher velocity dispersions and distorted velocity fields suggesting outflows;

(iii) Signatures of outflows are mostly observed in the [Fe II] kinematics of NGC 788, NGC 3227, NGC 3516, NGC 5506, NGC 5899. The modelling of the gas kinematics and quantification of the mass outflow rates and powers will be presented in a forthcoming paper (Paper B);

(iv) There is usually an inverse correlation between the h_3 Gauss–Hermite moment and the velocity field: positive values (red wings) are associated with blueshifts and negative values (blue wings) are associated with redshifts. This can be understood as due to the gas rotating closer to the galaxy plane originating the 'main' velocity field – corresponding to the emission line peaks, while tenuous gas at higher latitudes rotating with lower velocities originate the 'lagging' wings;

(v) There is in some cases also an inverse correlation between h_4 and the velocity dispersion maps: low values of σ correspond to positive values of h_4 (peaky profiles with extended wings), while high σ values correspond to negative values of h_4 (boxy profiles). We see mostly positive h_4 values, which we attribute to gas rotating in the disc (low σ), on which less luminous emission of hotter gas at higher latitudes gives origin to the broad wings;

(vi) Although the excitation will be further analysed in Paper B, general trends observed in the emission line ratios are: (1) an increase in [Fe II] λ1.2570 μm/Pa β in association with higher velocity dispersion indicating contribution from shocks, and an increase in $H_2\,\lambda\,2.12\mu$m/Br γ outwards, attributed to destruction of the H_2 molecule close to the AGN due to its strong radiation;

(vii) The integrated mass of ionized gas within the inner ≈300 pc radius ranges from 1.8×10^5 to 1.9×10^7 $M_\odot$, while that of warm molecular gas is $\sim 10^{3-4}$ times lower, and the estimated mass in cold molecular gas is $\sim 10^2$ times higher;

(viii) The average ionized gas surface mass density ranges from 2.8 to 140 $M_\odot$ pc^{-2}, while for the warm molecular gas it is $\sim 10^{3-4}$ times lower, and that estimated for the cold molecular gas is $\sim 10^2$ times higher.

(ix) The AGN accretion rates in our sample range from 0.1×10^{-3} to $49 \times 10^{-3} M_\odot$ yr^{-1}; considering an activity cycle of duration 10^7–10^8 yr, it can be concluded that there are $\approx 10^2$ times more gas in the inner few 100 pc of the galaxies than needed to feed the AGN over a duty cycle;

(x) If most of this gas will lead to star formation in the inner few 100 pc, we estimate SFRs in the range 1–260 $\times$ 10^{-3} $M_\odot$ yr^{-1} which is within the range of typical values observed for circumnuclear star-forming regions in nearby galaxies;

(xi) The mass reservoirs in the inner few 100 pc of these galaxies are thus enough to power both the central AGN and star formation. But our observations show also that at least part of this gas is being pushed away by an AGN-driven outflow or supernovae winds, which we will further investigate via the analysis of the gas kinematics in Paper B.

This paper is the thirteenth of a series by our group AGNIFS in which we have been mapping in detail AGN feeding and feedback processes in nearby galaxies using AO assisted integral field observations with NIFS. And it is the third in which we aim to characterize a global sample of 20 nearby active galaxies, the first one in which we characterized the stellar kinematics (Riffel et al. 2017) and the second in which we presented the sample and mass density profiles (Riffel et al. 2018). The observations are scheduled to be concluded in 2019. Further and more detailed analysis of the gas kinematics and excitation for the six galaxies presented in this work will be presented in the forthcoming Paper B.

ACKNOWLEDGEMENTS

We thank an anonymous referee for valuable suggestions which helped to improve the paper. This study was financed in part by the Coordenação de Aperfeiçoamento de Pessoal de Nível Superior - Brasil (CAPES) - Finance Code 001, Conselho Nacional de Desenvolvimento Científico e Tecnológico (CNPq) and Fundação de Amparo à pesquisa do Estado do RS (FAPERGS). This work is based on observations obtained at the Gemini Observatory, which is operated by the Association of Universities for Research in Astronomy, Inc., under a cooperative agreement with the NSF on behalf of the Gemini partnership: the National Science Foundation (United States), the Science and Technology Facilities Council (United Kingdom), the National Research Council (Canada), CONICYT (Chile), the Australian Research Council (Australia), Ministério da Ciência e Tecnologia (Brazil), and south-east CYT (Argentina).

REFERENCES

Aoki K., Ohtani H., Yoshida M., Kosugi G., 1994, PASJ, 46, 539
Arribas S., Mediavilla E., 1994, ApJ, 437, 149
Arribas S., Mediavilla E., García-Lorenzo B., del Burgo C., 1997, ApJ, 490, 227
Baillard A. et al., 2011, A&A, 532, A74
Barbosa F. K. B., Storchi-Bergmann T., McGregor P., Vale T. B., Rogemar Riffel A., 2014, MNRAS, 445, 2353
Binney J., Tremaine S., 1987, Galactic dynamics. Princeton University Press, Princeton, NJ
Blanco P. R., Ward M. J., Wright G. S., 1990, MNRAS, 242, 4P
Burtscher L. et al., 2015, A&A, 578, A47
Cardelli J. A., Clayton G. C., Mathis J. S., 1989, ApJ, 345, 245
Colbert E. J. M., Baum S. A., Gallimore J. F., O'Dea C. P., Lehnert M. D., Tsvetanov Z. I., Mulchaey J. S., Caganoff S., 1996, ApJS, 105, 75
Cruz-Gonzalez I., Carrasco L., Serrano A., Guichard J., Dultzin-Hacyan D., Bisiacchi G. F., 1994, ApJS, 94, 47
Dale D. A., Sheth K., Helou G., Regan M. W., Hüttemeister S., 2005, AJ, 129, 2197
Davies R. I., Maciejewski W., Hicks E. K. S., Tacconi L. J., Genzel R., Engel H., 2009, ApJ, 702, 114
Davies R. I. et al., 2014, ApJ, 792, 101
de Vaucouleurs G., de Vaucouleurs A., Corwin H. G. Jr, Buta R. J., Paturel G., Fouqué P., 1991, Third Reference Catalogue of Bright Galaxies. Springer-Verlag, New York, NY

Diniz M. R., Riffel R. A., Storchi-Bergmann T., Winge C., 2015, MNRAS, 453, 1727
Diniz M. R., Riffel R. A., Dors O. L., 2018, Res. Notes Am. Astron. Soc., 2, 3
Dors O. L. Jr, Storchi-Bergmann T., Riffel R. A., Schimdt A. A., 2008, A&A, 482, 59
Emonts B. H. C., Colina L., Piqueras-López J., Garcia-Burillo S., Pereira-Santaella M., Arribas S., Labiano A., Alonso-Herrero A., 2017, A&A, 607, A116
Evans I. N., Koratkar A. P., Storchi-Bergmann T., Kirkpatrick H., Heckman T. M., Wilson A. S., 1996, ApJS, 105, 93
Fabian A. C., 2012, ARA&A, 50, 455
Falcón-Barroso J., Ramos Almeida C., Böker T., Schinnerer E., Knapen J. H., Lançon A., Ryder S., 2014, MNRAS, 438, 329
Ferrarese L., Ford H., 2005, Space Sci. Rev., 116, 523
Ferruit P., Wilson A. S., Mulchaey J., 2000, ApJS, 128, 139
Goad J. W., Gallagher J. S. III, 1987, AJ, 94, 640
Goad J. W., Gallagher J. S. III, 1988, AJ, 95, 948
Hamuy M., Maza J., 1987, A&AS, 68, 383
Heckman T. M., Blitz L., Wilson A. S., Armus L., Miley G. K., 1989, ApJ, 342, 735
Heckman T. M., Kauffmann G., Brinchmann J., Charlot S., Tremonti C., White S. D. M., 2004, ApJ, 613, 109
Hopkins P. F., Torrey P., Faucher-Giguère C.-A., Quataert E., Murray N., 2016, MNRAS, 458, 816
Ho L. C., Filippenko A. V., Sargent W. L. W., 1997, ApJS, 112, 315
Huchra J. P., Wyatt W. F., Davis M., 1982, AJ, 87, 1628
Ilha G. d. S., Bianchin M., Riffel R. A., 2016, Ap&SS, 361, 178
Kay L. E., 1994, ApJ, 430, 196
Kennicutt R. C. Jr, 1998, ARA&A, 36, 189
Kewley L. J., Heisler C. A., Dopita M. A., Lumsden S., 2001, ApJS, 132, 37
Koratkar A. et al., 1996, ApJ, 470, 378
Kormendy J., Ho L. C., 2013, ARA&A, 51, 511
Kriss G. A., Espey B. R., Krolik J. H., Tsvetanov Z., Zheng W., Davidsen A. F., 1996, ApJ, 467, 622
Maiolino R., Stanga R., Salvati M., Rodriguez Espinosa J. M., 1994, A&A, 290, 40
Malkan M. A., Gorjian V., Tam R., 1998, ApJS, 117, 25
Markwardt C. B., 2009, in Bohlender D. A., Durand D., Dowler P., eds, ASP Conf. Ser. Vol. 411, Astronomical Data Analysis Software and Systems XVIII. Astron. Soc. Pac., San Francisco, p. 251
Martini P., Regan M. W., Mulchaey J. S., Pogge R. W., 2003, ApJS, 146, 353
Mazzalay X. et al., 2013, MNRAS, 428, 2389
Mazzalay X. et al., 2014, MNRAS, 438, 2036
McGregor P. J. et al., 2003, in Iye M., Moorwood A. F. M., eds, Proc. SPIE Conf. Ser. Vol. 4841, Instrument Design and Performance for Optical/Infrared Ground-based Telescopes. SPIE, Bellingham, p. 1581
Mulchaey J. S., Tsvetanov Z., Wilson A. S., Perez-Fournon I., 1992, ApJ, 394, 91
Müller Sánchez F., Davies R. I., Eisenhauer F., Tacconi L. J., Genzel R., Sternberg A., 2006, A&A, 454, 481
Müller Sánchez F., Davies R. I., Genzel R., Tacconi L. J., Eisenhauer F., Hicks E. K. S., Friedrich S., Sternberg A., 2009, ApJ, 691, 749
Mundell C. G., Holloway A. J., Pedlar A., Meaburn J., Kukula M. J., Axon D. J., 1995, MNRAS, 275, 67
Mundell C. G., James P. A., Loiseau N., Schinnerer E., Forbes D. A., 2004, ApJ, 614, 648
Nagar N. M., Wilson A. S., Mulchaey J. S., Gallimore J. F., 1999, ApJS, 120, 209
Nagar N. M., Oliva E., Marconi A., Maiolino R., 2002, A&A, 391, L21
Osterbrock D. E., Ferland G. J., 2006, Astrophysics of gaseous nebulae and active galactic nuclei. Calif: University Science Books, Sausalito
Prugniel P. et al., 2001, in Banday A. J., Zaroubi S., Bartelmann M., eds, Mining the Sky. Springer-Verlag, Berlin, p. 683
Ramos Almeida C. et al., 2009, ApJ, 702, 1127
Riffel R. A., 2010, Ap&SS, 327, 239
Riffel R. A., Storchi-Bergmann T., Winge C., Barbosa F. K. B., 2006, MNRAS, 373, 2
Riffel R. A., Storchi-Bergmann T., Winge C., McGregor P. J., Beck T., Schmitt H., 2008a, MNRAS, 385, 1129
Riffel R., Pastoriza M. G., Rodríguez-Ardila A., Maraston C., 2008b, MNRAS, 388, 803
Riffel R. A., Storchi-Bergmann T., Dors O. L., Winge C., 2009a, MNRAS, 393, 783
Riffel R., Pastoriza M. G., Rodríguez-Ardila A., Bonatto C., 2009b, MNRAS, 400, 273
Riffel R. A., Storchi-Bergmann T., McGregor P. J., 2009c, ApJ, 698, 1767
Riffel R. A., Storchi-Bergmann T., Nagar N. M., 2010a, MNRAS, 404, 166
Riffel R. A., Storchi-Bergmann T., Riffel R., Pastoriza M. G., 2010b, ApJ, 713, 469
Riffel R. A., Storchi-Bergmann T., 2011a, MNRAS, 417, 2752
Riffel R., Riffel R. A., Ferrari F., Storchi-Bergmann T., 2011b, MNRAS, 416, 493
Riffel R. A., Storchi-Bergmann T., Winge C., 2013, MNRAS, 430, 2249
Riffel R. A., Vale T. B., Storchi-Bergmann T., McGregor P. J., 2014a, MNRAS, 442, 656
Riffel R. A., Storchi-Bergmann T., Riffel R., 2014b, ApJ, 780, L24
Riffel R. A., Storchi-Bergmann T., Riffel R., 2015, MNRAS, 451, 3587
Riffel R. A. et al., 2016, MNRAS, 461, 4192
Riffel R. A., Storchi-Bergmann T., Riffel R., Dahmer-Hahn L. G., Diniz M. R., Schönell A. J., Dametto N. Z., 2017, MNRAS, 470, 992
Riffel R. A. et al., 2018, MNRAS, 474, 1373
Roche P. F., Aitken D. K., Smith C. H., Ward M. J., 1991, MNRAS, 248, 606
Roche P. F., Packham C., Aitken D. K., Mason R. E., 2007, MNRAS, 375, 99
Rodríguez-Ardila A., Contini M., Viegas S. M., 2005, MNRAS, 357, 220
Schinnerer E., Eckart A., Tacconi L. J., 2000, ApJ, 533, 826
Schmidt M., 1959, ApJ, 129, 243
Schmitt H. R., Kinney A. L., 2000, ApJS, 128, 479
Schönell A. J., Riffel R. A., Storchi-Bergmann T., Winge C., 2014, MNRAS, 445, 414
Schönell A. J. Jr, Storchi-Bergmann T., Riffel R. A., Riffel R., 2017, MNRAS, 464, 1771
Scoville N. Z., Hall D. N. B., Ridgway S. T., Kleinmann S. G., 1982, ApJ, 253, 136
Shi L., Gu Q. S., Peng Z. X., 2006, A&A, 450, 15
Siebenmorgen R., Krügel E., Spoon H. W. W., 2004, A&A, 414, 123
Somerville R. S., Hopkins P. F., Cox T. J., Robertson B. E., Hernquist L., 2008, MNRAS, 391, 481
Springel V., Di Matteo T., Hernquist L., 2005, MNRAS, 361, 776
Storchi-Bergmann T., Schnorr-Müller A., 2019, Nat. Astron., 3, 48
Storchi-Bergmann T., McGregor P. J., Riffel R. A., Simões Lopes R., Beck T., Dopita M., 2009, MNRAS, 394, 1148
Storchi-Bergmann T., Lopes R. D. S., McGregor P. J., Riffel R. A., Beck T., Martini P., 2010, MNRAS, 402, 819
Storchi-Bergmann T., Riffel R. A., Riffel R., Diniz M. R., Borges Vale T., McGregor P. J., 2012, ApJ, 755, 87
Terrazas B. A., Bell E. F., Henriques B. M. B., White S. D. M., Cattaneo A., Woo J., 2016, ApJ, 830, L12
Tsai M., Hwang C.-Y., 2015, AJ, 150, 43
Ulrich M.-H., Pequignot D., 1980, ApJ, 238, 45
Ulvestad J. S., Wilson A. S., 1989, ApJ, 343, 659
Veilleux S., Tully R. B., Bland-Hawthorn J., 1993, AJ, 105, 1318
Voit G. M., Shull J. M., Begelman M. C., 1987, ApJ, 316, 573
Wagner S. J., 1988, PASP, 100, 54
Westfall K. B., Bershady M. A., Verheijen M. A. W., Andersen D. R., Swaters R. A., 2007, Astrophys. Space Sci. Proc., 3, 157
Zaw I., Farrar G. R., Greene J. E., 2009, ApJ, 696, 1218

This paper has been typeset from a TEX/LATEX file prepared by the author.